Various regimes of charge-density waves in layered compounds

G. P. E. M. Van Bakel and J. Th. M. De Hosson
Department of Applied Physics, Materials Science Centre, University of Groningen, Zernike Complex, Nijenborgh 4, 9747 AG Groningen, The Netherlands
(Received 11 December 1991)

In this paper we have subjected different layered transition-metal dichalcogenides to scanning tunneling microscopy to reveal the electronic charge distribution associated with the charge-density-wave (CDW) part of the superstructure, in addition to the atomic corrugation. The observations presented display three regimes ranging from a localized CDW centered around defects or impurities in the case of $1T$-TiS_2, via an intermediate regime governed by overlapping envelope functions in $2H$-$NbSe_2$, to a fully developed CDW in $1T$-$TaSe_2$ (as well as in a large number of other compounds). We have obtained strong indication from both direct-space observations and comparison to calculated images based upon the Ginzburg-Landau theory that localized charge-density waves do exist in conjunction with associated lattice distortions. The fact that these observations have been made in solids ranging from (dirty) semiconductor ($1T$-TiS_2) to semimetal ($1T$-$TaSe_2$) to metallic ($2H$-$NbSe_2$) points to the general applicability of the phenomenological Ginzburg-Landau theory, employed to describe the various regimes in which the formation of charge-density waves and the accompanying periodic lattice distortions appear to act.

I. INTRODUCTION

A large number of layered transition-metal dichalcogenides (LTMD) exhibit first-order phase transitions, having a marked effect on electrical conductance, Hall coefficient, and magnetic susceptibility. For nearly two decades, charge-density waves (CDW) and the accompanying periodic lattice distortion (PLD) in layered transition-metal compounds are held responsible for these effects.[1,2]

CDW appear to occur in a number of two-dimensional layered compounds such as TaS_2, $TaSe_2$, and $NbSe_2$. The former two appear in the so-called $1T$ phase as well as in the so-called $2H$ structure. In the $1T$ structure the metal ion is octahedrally coordinated, whereas in the $2H$ structure the metal ion is trigonal-prismatically coordinated. $NbSe_2$ exhibits only the $2H$ polytype structure.

Above some critical temperature global CDW are absent and this is referred to as the normal state. Below this temperature a CDW is present, the wave vectors of which are not low-integer rational fractions of the crystal-lattice reciprocal vectors [incommensurate charge-density wave (ICDW)]. At even lower temperature the wave vectors become commensurate, spanning a perfect superlattice [commensurate charge-density wave (CCDW)]. The transition ICDW-CCDW is of a first-order nature and may show complicated behavior and hysteresis may be present. This has been attributed to CDW domains in which the overall ICDW is divided into commensurate domains separated by domain walls in which there is a phase-angle discontinuity.[3] The first-order transition temperatures of $1T$-$TaSe_2$ and $1T$-TaS_2 are 473 and 150 K, respectively. The scanning tunneling microscope (STM) is sensitive to both atomic arrangements and electronic structure. However, in the case of CDW/PLD it is generally the condensation of conduction-electron charge density the resulting image will be influenced by to the greatest extent, rather than the shift in position of the atomic centers, generally being small with respect to the interatomic distance. This is in contrast to, for instance, x-ray diffraction, where displacements in the atomic positions contribute to the diffraction patterns. The periodic lattice distortion is only manifest at the discrete lattice sites and this results in diffraction spots accompanied by satellites. The time average of the electronic charge density, however, is a continuous function of spatial coordinates and when measured in real space will result in a topograph of the distribution. The question whether the STM indeed acts as a device that measures the local electronic charge density was treated by Tersoff.[4] In this case the tip-sample junction can be regarded as acting in the tunneling regime and the spread of the Fermi distribution is small (i.e., zero temperature) and the tip-sample bias voltage is low. The tunneling current is calculated using first-order perturbation theory

$$J \propto \frac{4\pi^2 e^2 V}{h} \sum_{\mu,\nu} |M_{\mu\nu}|^2 \delta(E_\nu - E_F)\delta(E_\mu - E_F) , \qquad (1)$$

where μ and ν denote electronic states in tip and sample, respectively. E_F denotes the Fermi energy and $M_{\mu,\nu}$ is the tunneling matrix element. When the tunneling probe can be modeled by a δ distribution, then the expression reduces to

$$J \propto \sum_{\nu} |\Psi_\nu(\mathbf{r})|^2 \delta(E_\nu - E_F) . \qquad (2)$$

The right-hand side of expression (2) equals the local density of states at the Fermi level, which is proportional to the conduction-electron charge density. From this it is concluded that the tunneling current, determined by the local density of states at the Fermi level, probes the conduction-electron charge density as a function of spatial coordinate. Direct measurement of the charge-

density wave, superimposed on the periodic charge density due to the atomic lattice, is therefore possible.

Since the STM is able to make observations in direct space, localized distortions in the CDW will then immediately become evident from the observations. Therefore the scanning tunneling microscope is an instrument well suited for studies of the charge-density waves existing in solids and the real-space high-resolution capabilities of this instrument makes it a powerful tool in the investigation of the effect of defects and/or impurities on the CDW. The flat cleavage surface makes the LTMD especially suitable for examination by STM.

Various authors have investigated the effect of defects and/or impurities on CDW/PLD formation with pulsed NMR and electron diffraction and this has resulted in the recognition of the onset of CDW/PLD formation above the temperature for which the system undergoes a phase transition.[5–8] Chemical substitution has led to distorted CDW as seen by the scanning tunneling microscope.[9–12]

Here we present STM results on a number of LTMD compounds, belonging to different regimes as far as crystal symmetry and electronic transport properties are concerned. Firstly, results on $1T$-$TaSe_2$ are presented. In $1T$-$TaSe_2$ the Ta atoms are octahedrally coordinated by the Se. A transition from CCDW to ICDW develops at 473 K whereas at about 600 K the structure transforms to a different polytype ($2H$-$TaSe_2$) and the transition from ICDW to normal is therefore absent. The CCDW has periodicity equal to $3\mathbf{a}-\mathbf{b}$ and $\mathbf{a}$ and $\mathbf{b}$ denote primitive vectors, 120° apart, spanning the surface crystal lattice. This rotation costs less energy than a change in wavelength of the CDW which could result in a $3\mathbf{a}\times 3\mathbf{b}$ superlattice. The electric conductivity is governed by the semimetallic character. Secondly, $1T$-TiS_2 is discussed. This material is a "dirty" semiconductor with a small band gap and is close to semimetallic behavior. No global CDW formation is known to exist in this material at any temperature. The Ti atoms are in octahedral coordination; this implies existence of two kinds of tetrahedral vacancy sites next to octahedral sites fully occupied by Ti in the perfect crystal and a double number of octahedral vacancies in the van der Waals gap in between adjacent sandwiches. The dirty semiconductor behavior points at intrinsic defects, probably displaced Ti atoms. Thirdly, $2H$-$NbSe_2$ crystals are investigated. This material is metallic and the Nb atom has trigonal prismatic coordination. An ICDW develops at 33 K, with an almost $3\mathbf{a}\times 3\mathbf{b}$ structure. Below 7 K $2H$-$NbSe_2$ becomes superconducting and CDW formation and superconductivity coexist.

II. THEORETICAL CONCEPTS

Since the phase transformations in the sequence normal-ICDW-CCDW are "weak" first-order transitions, McMillan[13] has employed the Ginzburg-Landau theory[14] to describe these phenomena. It forms the basic tool in our analysis and therefore it will be summarized in a concise way. Recognizing the fact that experiments show three charge-density waves that have components 120° apart, McMillan introduces a six-component order parameter consisting of three complex functions $\psi_i(\mathbf{r})$. These are related to the conduction-electron charge density by

$$\rho(\mathbf{r})=\rho_0(\mathbf{r})[1+\alpha(\mathbf{r})] , \tag{3}$$

where $\rho_0(\mathbf{r})$ is the charge density in the normal state and

$$\alpha(\mathbf{r})=\mathrm{Re}\{\psi_1(\mathbf{r})+\psi_2(\mathbf{r})+\psi_3(\mathbf{r})\} . \tag{4}$$

Now the free-energy density must be constructed. The simplest form to start with is the "Landau" part of the free-energy density: $a\alpha^2+b\alpha^3+c\alpha^4+\cdots$, where the cubic term must be included to describe a first-order transition. This expression, however, does not permit a distinction between single and triple charge-density waves. Therefore cross terms are added of the form $d(|\psi_1\psi_2|^2+|\psi_2\psi_3|^2+|\psi_3\psi_1|^2)$. The gradient terms are chosen such that the free energy is a minimum when the wave vectors of the CDW correspond to those observed

$$e\sum_{i=1}^{3}|(\mathbf{q}_i\cdot\nabla-i\mathbf{q}_i^2)\psi_i|^2+f\sum_{i=1}^{3}|\mathbf{q}_i\times\nabla\psi_i|^2 . \tag{5}$$

Here $|\mathbf{q}_i|=2\pi/\lambda$, where λ represents the wavelength of the incommensurate CDW and the directions lie in the plane separated by 120°. The coefficients e and f refer to the "elastic constants" of the CDW. The particular $\mathbf{q}_i$'s are related to the geometry of the Fermi surface. All the coefficients $a,b,\ldots,$ etc. must have the periodicity of the lattice, e.g.,

$$a(\mathbf{r})=a_0+a_1\sum_i\exp(i\mathbf{K}_i\cdot\mathbf{r}) , \tag{6}$$

where $\mathbf{K}_i$ is one of the six shortest reciprocal-lattice vectors of the hexagonal planar lattice. If $d_0>9c_0/4$, the triple CDW will be more stable than a single CDW.

Now, the total energy can be minimized with respect to variations in the order parameter, i.e., the total energy of one layer (integration of the Landau expression of the total energy over $d^2\mathbf{r}$), is minimized with respect to variation in $\delta\psi$. The variations may be written out explicitly and set to zero. Like the zero-field solutions in the Ginzburg-Landau theory,[14] the solution of $\psi(\mathbf{r})$ of this differential equation is, beside the trivial solution of $\psi(\mathbf{r})=0$, a plane wave $\psi(\mathbf{r})=\psi_0\exp(i\mathbf{q}\cdot\mathbf{r})$. The coherence length is given by the square root of the ratio of the coefficient of the gradient term in the free energy to that of the quadratic term. Assuming an order parameter of the form $\psi_i(\mathbf{r})\cong\exp[i(\mathbf{q}_i+\mathbf{q})\cdot\mathbf{r}]$ with $\mathbf{q}\|\mathbf{q}_i$, the coherence length is given by

$$\xi=\left[\frac{2e_0q_i^2}{a_0}\right]^{1/2} , \tag{7}$$

where the total free energy can be written as (taking the crystal potential to be equal to zero)

$$\begin{aligned}F&=\sum_{\mathbf{q}}[\tfrac{1}{2}a_0+e_0(\mathbf{q}_i\cdot\mathbf{q})^2+f_0(\mathbf{q}_i\times\mathbf{q})^2]\psi_0^2\\&=\sum_{\mathbf{q}}g_{\mathbf{q}}\psi_0^2 .\end{aligned} \tag{8}$$

In the normal state the charge density is unaffected and

uniform. However, impurities may give rise to fluctuations in the order parameter. As a consequence $\psi_i(\mathbf{r})=\phi(\mathbf{r})\exp(i\mathbf{k}_i\cdot\mathbf{r})$, where $\mathbf{k}_i=\mathbf{q}_i$ for the incommensurate phase and $\mathbf{k}_i=\mathbf{K}_i/3$ for the commensurate phase. Both the coefficient $\phi(\mathbf{r})$ and the impurity potential $U(\mathbf{r})$ can be Fourier transformed, like

$$\phi(\mathbf{r})=\phi_0+\sum_{\mathbf{q}}\phi_{\mathbf{q}}e^{i\mathbf{q}\cdot\mathbf{r}} . \tag{9}$$

In Eq. (8) the contribution due to the impurity potential must be added to the free energy together with a change of ψ_0 by $\phi_{\mathbf{q}}$. Next, minimizing F with respect to $\phi_{\mathbf{q}}$, Eq. (9) can be rewritten for one impurity at the origin as

$$\psi_i(\mathbf{r})=\phi_0 e^{i\mathbf{q}_i\mathbf{r}}-\tfrac{1}{2}U_0\sum_{\mathbf{q}}\frac{e^{i(\mathbf{q}+\mathbf{q}_i)\cdot\mathbf{r}}}{g_{\mathbf{q}}} . \tag{10}$$

Combining Eq. (10) with (3) the expression for the charge density around one impurity is given by[13] (assuming e_0 to be equal to f_0)

$$\rho(\mathbf{r})=\rho_0(\mathbf{r})\left[1-\sum_{i=1}^{3}\frac{u_0\cos(\mathbf{q}_i\cdot\mathbf{r})f(r/\xi)}{4\pi e_0 q_i^2}\right] . \tag{11}$$

This equation is valid for $\mathbf{q}_i\cdot\mathbf{r}>1$. The function $f(r/\xi)$ is expressed as an integral

$$f(r/\xi)=\int_1^{\infty}\frac{e^{-yr/\xi}}{(y^2-1)^{1/2}}dy . \tag{12}$$

This is an improper integral for the integrand approaches infinity when y approaches 1 and the integration interval is infinite. However, the integrand may be approximated for low and high values of y and the contributions of the lower and upper part of the integration interval are readily estimated. The contributions of the intermediate values of y can be calculated numerically. This procedure may be carried out for various values of r/ξ. The function $f(r/\xi)$ shows an asymptotic behavior according to

$$f(r/\xi)=\begin{cases}\ln(1.12\xi/r), & r/\xi\ll 1 \quad (13)\\ \left[\dfrac{\pi\xi}{2r}\right]^{1/2}e^{-r/\xi}, & r/\xi\gg 1 . \quad (14)\end{cases}$$

The numerically calculated values then can be checked against this asymptotic behavior. The function $f(r/\xi)$ is displayed in Fig. 1. The resulting expression for the charge density contains only a few parameters.

III. EXPERIMENTS

In order to obtain topographic maps of the conduction-electron density, samples of the materials under investigation were subjected to imaging in the scanning tunneling microscope operated in air, at room temperature, and at relatively low-bias-voltage condition. The actual bias voltages times the electron charge being in the order of kT at room temperature, the imaging can be regarded as being performed at nearly zero bias. In the low-voltage regime, according to Tersoff,[4] the tunneling current is to be interpreted as a measure of the conduction-electron charge density. The tunneling current was kept at a value of approximately 1 nA and was adjusted to give stable and reproducible images. The exponential dependence of the tunneling current versus tip-sample distance indicates that the junction can be regarded as operating in the tunneling regime (see Fig. 2). The samples were grown by the vapor-transport method using iodine as the transport agent. Prior to imaging the samples were cleaved in air, resulting in atomically flat surfaces. The microscope used was a commercially available instrument without modifications.[15]

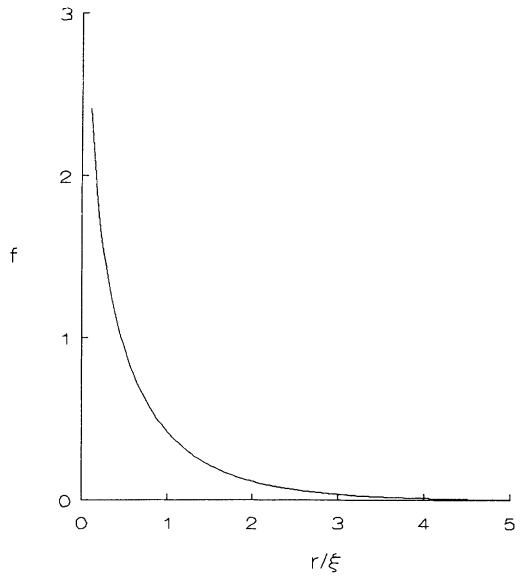

FIG. 1. Plot of envelope function $f(r/\xi)$.

A. 1T-$TaSe_2$

Imaging of 1T-$TaSe_2$ revealed the characteristic superposition of atomic and CDW corrugation, depicted in Fig. 3. The measured angles between the lattices and the ratio of the lattice parameters agree with those observed earlier.[16–18] The simultaneous appearance of the two corrugations is due to the fact that the amplitudes of the two corrugations are about equal. This is not a general result of all the transition metal dichalcogenides. It is to be mentioned that one of the CDW maxima is depressed

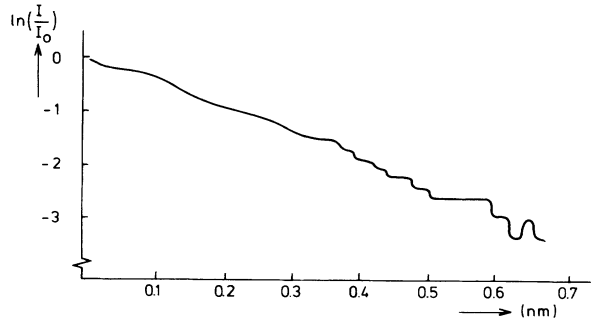

FIG. 2. Logarithm of tunneling current vs tip-sample separation at $V_{\text{sample}}-V_{\text{tip}}=25$ mV for a TiS_2 sample and tungsten tip.

with respect to the average amplitude; however, the atomic lattice shows it to be unaffected by this effect. This indicates that a disturbance of the CDW corrugation does not necessarily have an effect on the atomic corrugation. The CDW corrugation in this example is described well by the equations in the section of this paper concerning the Landau theory when only a periodic lattice potential is present. However, this does not hold for the missing CDW maximum and this points at distortion of the CDW lattice caused by the presence of defects.

B. 1*T*-TiS_2

Earlier results of STM topographs of 1*T*-TiS_2 have been reported in Refs. 19 and 20. In our previous paper[20] a connection was made with the presence of interstitial atoms and vacancies. Here, based on the Ginzburg-Landau theory, we establish a calculation of the appearance of impurity-induced localized charge-density waves. The observed features are depicted again in Fig. 4 and are referred to as type 1, type 6, and type 15, respectively (the nomenclature is based on the number of image spots differing in intensity from the overall atomic corrugation).

Equation (11) is taken as a starting point for the calculation of STM topographs. To model the atomic corrugation a superposition of three plane waves is taken, with wave vectors being equal in size and having an angular separation of 120°. The wave vectors add to zero, ensuring the maxima to coincide at a two-dimensional Bravais lattice (hexagonal). The charge-density map obtained corresponds to the observed corrugation to a fair degree. The full expression for the calculated images is given by

$$h(\mathbf{r}) = A_{\text{lat}} \sum_{i=1}^{3} \cos[\mathbf{K}_i \cdot (\mathbf{r}+\mathbf{d}_{\text{lat}})] + A_{\text{CDW}} f\left[\frac{[(|\mathbf{r}|^2+z^2)]^{1/2}}{\xi}\right] \times \sum_{i=1}^{3} \cos[\mathbf{q}_i \cdot (\mathbf{r}+\mathbf{d}_{\text{CDW}})+\theta_{\text{CDW}}] , \quad (15)$$

with conditions $\sum_i^3 \mathbf{K}_i = 0$ and $\sum_i^3 \mathbf{q}_i = 0$.

In all the calculations each set of the wave vectors, either $\mathbf{K}_i$ or $\mathbf{q}_i$, consists of a star of vectors of equal length and 120° apart. The two vector sets have the same orientation. By taking the vectors composing the localized charge-density wave as somewhat smaller than half the ones used to generate the atomic corrugation and adjusting the amplitude, location, and correlation length, topographs are assembled that do resemble the observed features in the case of type 1 and type 6. For a full account of the parameters used in Figs. 5–7, see Table I. For type 15, much smaller wave vectors were applied and also a phase shift was introduced, resulting in a topograph in reasonable agreement with the observed type feature.

For all three features, the origin of the envelope function was chosen below the surface, at a distance in agreement with the assumed defect sites. The signs of the amplitudes correspond to the defect model in which type 2 and type 6 are ascribed to titanium interstitials and type 15 as a vacancy at a lattice site normally occupied by titanium. In fact the calculated images for type 1 and type 6 only differ in the position of the origin of the CDW system.

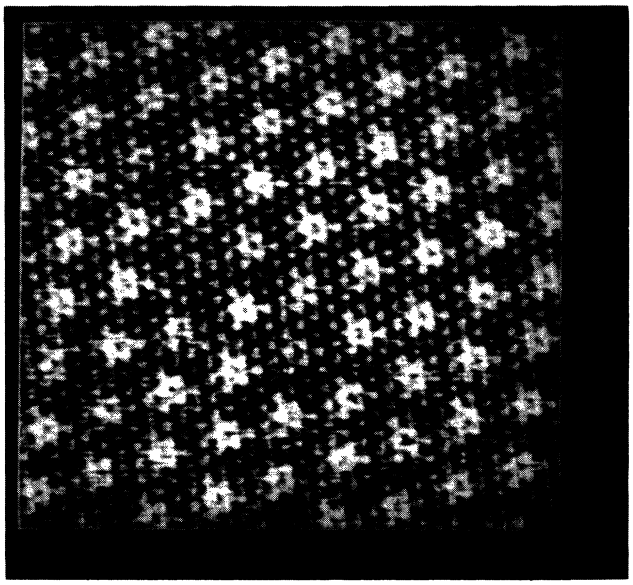

FIG. 3. STM constant-height image of 1*T*-$TaSe_2$ at $V_{\text{sample}} - V_{\text{tip}} = 3.1$ mV and $I_{\text{set point}} = 2.4$ nA.

C. 2*H*-$NbSe_2$

STM topographs of 2*H*-$NbSe_2$ were reported before by Dahn *et al.*[21] and "buckling of the surface with a period of several times the interatomic spacing" was mentioned. The STM images presented here allow us to make a more careful analysis of this buckling and its possible relation to charge-density waves. From the constant height map,

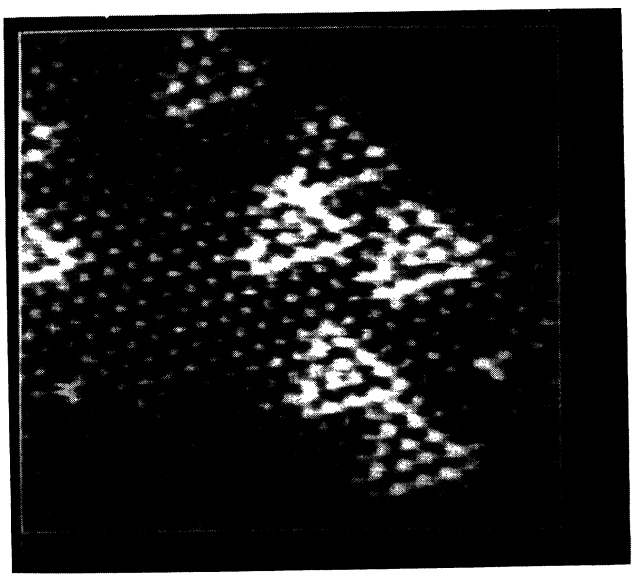

FIG. 4. STM constant-current image of 1*T*-TiS_2 at $V_{\text{sample}} - V_{\text{tip}} = 25$ mV and $I_{\text{set point}} = 1.3$ nA.

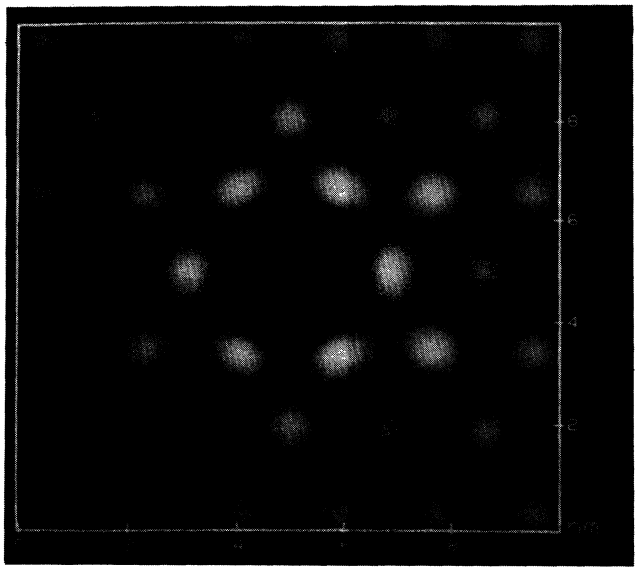

FIG. 5. Calculated STM image of a type-1 feature.

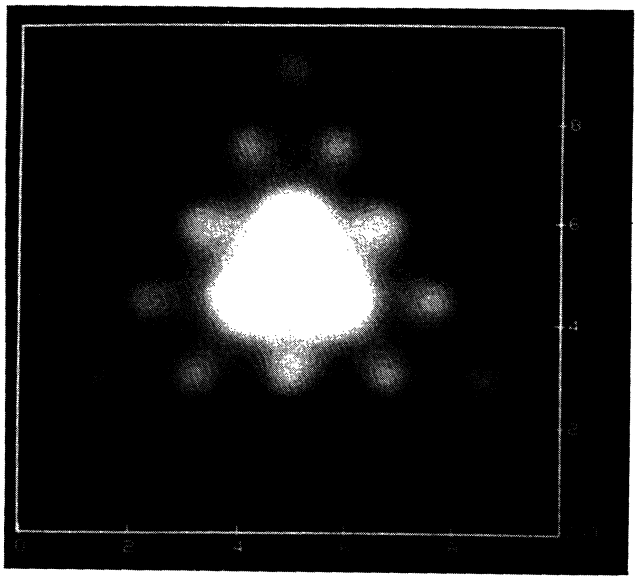

FIG. 7. Calculated STM image of a type-15 feature.

shown in Fig. 8, it is clear that, apart from the atomic corrugation, whose lattice has the appropriate spacing and symmetry, a number of atomic sites displays larger tunneling probability (bright contrast) than the average amplitude, whereas an about equal number displays the opposite behavior (dark contrast). Furthermore, there seems to be a correspondence between the tunneling current amplitudes of alternate atomic rows. To make this statement more quantitative, the autocorrelation function was calculated, as depicted in Fig. 9. This (real) function shows the correlation between sites connected by a certain shift vector

$$G(\mathbf{s})=\int\int z(\mathbf{r})\cdot z(\mathbf{r}+\mathbf{s})d^2\mathbf{r}\ . \tag{16}$$

If the tunneling current map consists of the superposition of three plane waves, then the autocorrelation function

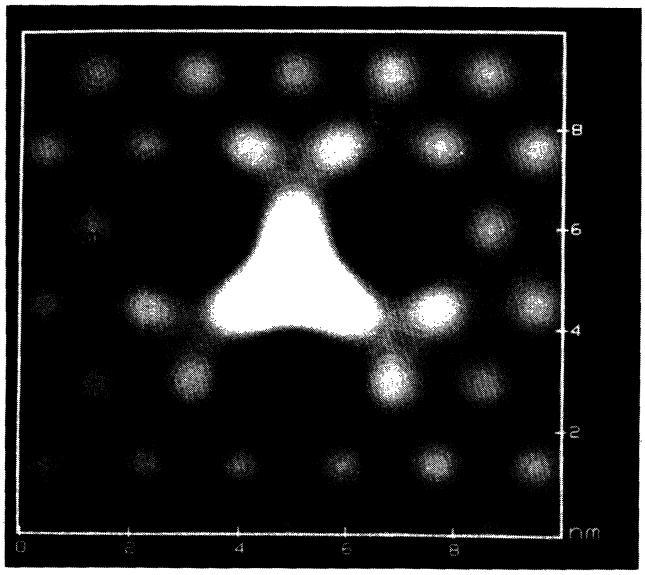

FIG. 6. Calculated STM image of a type-6 feature.

will take the same form. The measured autocorrelation values at the different nearest-neighbor separations are listed in Table II, taking the values at the center equal to 1. From Table II it can be derived that the next-nearest-neighbor correlation is larger than the nearest-neighbor correlation.

The comparison is feasible because the envelope of the correlation function shows little decay over many interatomic distances. The values of the correlations cannot be taken as absolute because the correlation depends on both the corrugation of the superstructure and the coverage of the surface area. Next to the autocorrelation function, the two-dimensional Fourier transform was performed, the intensity map of which is shown in Fig. 10. The spectrum can be divided into contributions from the atomic corrugation and the surface buckling, respectively. The atomic lattice has a well-defined period and the fundamental harmonic constituent gives rise to a hexagonally arranged set of bright spots. The spots outside this hexagon are due to the higher harmonics necessary to describe the observed current map. Inside the fundamental hexagon six clouds are visible, having the same symmetry as the spots belonging to the atomic lattice.

From the autocorrelation function we deduced that the next-nearest-neighbor correspondence is larger than the nearest-neighbor correspondence. The vector connecting next-nearest neighbors also connects alternate close-packed atomic rows. Alternate atomic rows are connected by a plane wave having a wave vector half that of the atomic lattice. Now suppose the observed current map consists of a superposition of the atomic corrugation and an electronic density corrugation described by a superposition of three plane waves. These waves are described by wave vectors that are about one-half of those describing the atomic corrugation. Their amplitudes are modulated by a modulation function containing spatial frequencies up to about one-half of the fundamental spatial frequency of the atomic lattice. The resulting Fourier transform

TABLE I. Parameters used in calculation of Figs. 5,6,7.

	Type 1	Type 6	Type 15
$\|\mathbf{K}\|$	2.131×10^{10} m^{-1}	2.131×10^{10} m^{-1}	2.131×10^{10} m^{-1}
$\|\mathbf{q}\|$	0.852×10^{10} m^{-1}	0.852×10^{10} m^{-1}	0.320×10^{10} m^{-1}
$\mathbf{d}_{lat}$	(0,0) nm	(0,−0.197) nm	(0,−0.197) nm
$\mathbf{d}_{CDW}$	(0,0) nm	(0,0.492) nm	(0,0) nm
θ	0	0	−1.100
ξ	0.224 nm	0.224 nm	0.352 nm
A_{CDW}/A_{lat}	−15	−15	15
z	0.209 nm	0.070 nm	0.141 nm

will consist of the fundamental hexagon due to the atomic lattice, a convolution of a hexagon, the size being one-half that of the fundamental one, and the Fourier transform of the modulation function. If the uniform "superlattice" having the double interatomic spacing is drawn in the observed image then it becomes clear that long-range correlation between alternate rows is absent and phase shifts of π are seen to occur often. Therefore this is certainly not a superstructure with large coherence length. So the modulation function (or functions when each plane wave is contributing to the superlattice is modulated by its own function) will have to introduce phase shifts. Now attention is drawn to the feature present in the $2H$-$NbSe_2$ map, resembling the type-6 feature in the case of $1T$-TiS_2. In the analysis of $1T$-TiS_2 it became clear that the phases of the plane waves are essential in establishing a matching calculated feature. Since this feature occurs more than once in the current map, the modulation functions probably originate from several sources, possibly impurities or defects in or at the $2H$-$NbSe_2$ crystal. On the other hand, phase shifts are also present in nearly commensurate charge-density waves[3,22–24] and a domain structure establishes in order to minimize total free energy. This, however, is not a very likely explanation for the observed phase shifts here, for the correlation length of the type-6 feature is short compared to the domain sizes encountered in incommensurate charge-density waves (say 30 interatomic distances). Decomposition of the modulation is difficult for the number of sources is seen to be rather high compared to the more or less isolated features in $1T$-TiS_2.

IV. DISCUSSION

CDW/PLD are known to exist in layered transition-metal compounds. The origin of these superstructures lies in the existence of (nearly) plane-parallel Fermi surfaces especially encountered in lower-dimensional materials. These Fermi surfaces are defined by virtue of the periodicity encountered in perfect crystals. Based on theory and experiments there is reason to believe that CDW/PLD can exist locally around impurities and/or defects. In this paper we have subjected different LTMD to scanning tunneling microscopy to reveal the electronic charge distribution associated with the CDW part of the superstructure, in addition to the atomic corrugation.

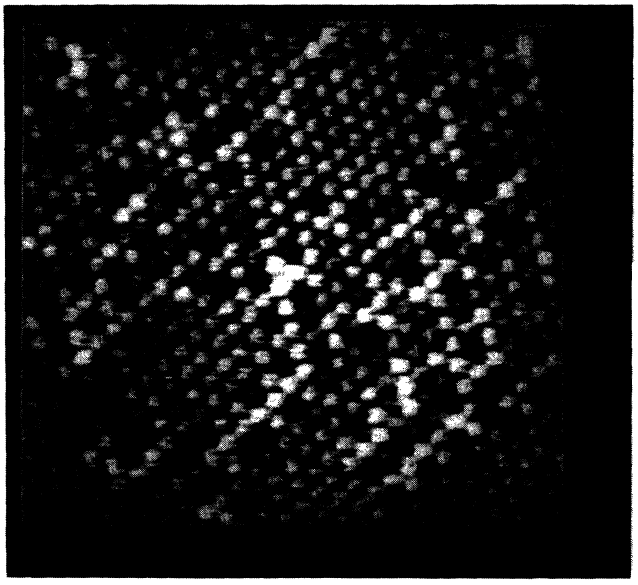

FIG. 8. STM constant-height image of $2H$-$NbSe_2$ at $V_{sample}-V_{tip}=5.8$ mV and $I_{set\ point}=1.0$ nA.

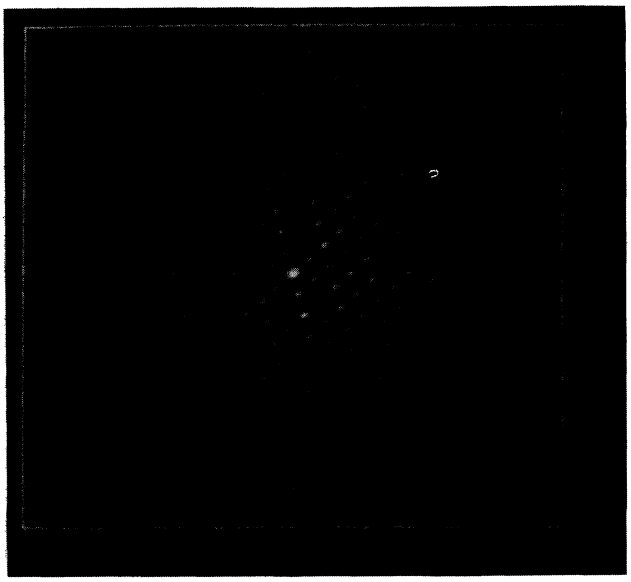

FIG. 9. Autocorrelation function corresponding to Fig. 8.

TABLE II. Autocorrelation values along close-packed directions in Fig. 9 (1, 2, and 3 refer to the nearest-, next-nearest, and third-nearest neighbors of the center 0).

	Position			
Angle	0	1	2	3
105°	1.00	0.386	0.448	0.404
345°	1.00	0.354	0.424	0.340
225°	1.00	0.368	0.452	0.340

We have obtained strong indication from both direct-space observations and comparison to calculated images based upon the Ginzburg-Landau theory, that indeed these localized charge-density waves exist in conjunction with associated lattice distortions. It has to be stressed that the superposition of waves presented here is two-dimensional in nature, whereas the actual crystal is three dimensional. However, we do not expect this to have a large effect on the results obtained because the extension to the third dimension only introduces small phase shifts and alters the wavelengths only to a small amount. Not included in the calculation are the possible effects of relaxation in the presence of a free surface. We do not believe the giant-corrugation theory treated by Tersoff,[25] in which imaging of a single wave vector is considered in the case of graphite, applies in the present case because the phenomena studied here are certainly not periodic. The results obtained indicate that the localized CDW not only can exist around impurities, but also around intrinsic defects. Care should be taken in the evaluation of these results since the actual defect type does not appear in these calculations, i.e., the defects are characterized only by a scalar (positive or negative) and a location.

The observations presented here display three regimes ranging from localized CDW/PLD centered around defects or impurities in the case of $1T$-TiS_2, via an intermediate regime governed by overlapping envelope functions in $2H$-$NbSe_2$, to a fully developed CDW/PLD system in $1T$-$TaSe_2$ (as well in a large number of other compounds). The fact that these observations have been made in solids ranging from (dirty) semiconductor ($1T$-TiS_2) to semimetal ($1T$-$TaSe_2$) to metallic ($2H$-$NbSe_2$) points at the general applicability of the phenomenological Ginzburg-Landau theory, employed to describe the various regimes in which CDW/PLD formation appears to act.

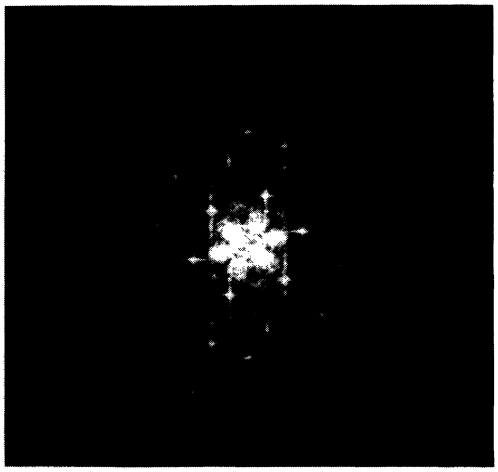

FIG. 10. Squared-amplitude two-dimensional Fourier transform corresponding to Fig. 8.

ACKNOWLEDGMENTS

This work is part of the research program of the Foundation for Fundamental Research on Matter (FOM–Utrecht) and has been made possible by financial support from the Netherlands Organization for Scientific Research (NWO–The Hague).

[1]J. A. Wilson, F. J. DiSalvo, and S. Mahajan, Adv. Phys. **24**, 117 (1975).
[2]R. H. Friend and A. D. Yoffe, Adv. Phys. **36**, 1 (1987).
[3]B. Burk, R. E. Thomson, A. Zettl, and J. Clark, Phys. Rev. Lett. **66**, 3040 (1991).
[4]J. Tersoff, in *Scanning Tunneling Microscopy and Related Methods,* edited by R. J. Behm, N. Garcia, and H. Rohrer (Kluwer Academic, Dordrecht, 1989), p. 77.
[5]H. Mutka and N. Housseau, Philos. Mag. A **47**, 797 (1983).
[6]H. Mutka, L. Zuppiroli, P. Molinie, and J. C. Bourgoin, Phys. Rev. B **23**, 5030 (1981).
[7]C. Berthier, D. Jerome, and P. Molinie, J. Phys. C **11**, 797 (1978).
[8]H. Mutka, N. Housseau, J. Pelissier, R. Ayroles, and C. Roucau, Solid State Commun. **50**, 161 (1984).
[9]H. Dai, H. Chen, and C. M. Lieber, Phys. Rev. Lett. **66**, 3183 (1991).
[10]H. Chen, X. L. Wu, and C. M. Lieber, J. Am. Chem. Soc. **112**, 3326 (1990).
[11]X. L. Wu and C. M. Lieber, Phys. Rev. B **41**, 1239 (1990).
[12]X. L. Wu, P. Zhou, and C. M. Lieber, Phys. Rev. Lett. **61**, 2604 (1988).
[13]W. L. McMillan, Phys. Rev. B **12**, 1187 (1975).
[14]V. L. Ginzburg and L. D. Landau, Nuovo Cimento **2**, 1234 (1955); R. M. White and T. H. Geballe, *Long Range Order in Solids* (Academic, New York, 1979), Suppl. 15, p. 47.
[15]Nanoscope II, Digital Instruments Inc., Santa Barbara, CA.
[16]C. G. Slough, W. W. McNairy, and R. V. Coleman, Phys. Rev. B **41**, 9255 (1990).
[17]R. V. Coleman, B. Giambattista, P. K. Hansma, A. Johnson, W. W. McNairy, and C. G. Slough, Adv. Phys. **37**, 559 (1988).
[18]G. Raina, K. Sattler, U. Mueller, N. Venkateswaran, and J. Xhie, J. Vac. Sci. Technol. B **9**, 1039 (1991).
[19]C. G. Slough, B. Giambattista, A. Johnson, W. M. McNairy, C. Wang, and R. V. Coleman, Phys. Rev. B **37**, 6571 (1988).
[20]G. P. E. M. van Bakel, J. Th. M. De Hosson, and T. Hibma, Appl. Phys. Lett. **56**, 2402 (1990).
[21]D. C. Dahn, M. O. Watanabe, B. L. Blackford, and M. H. Jericho, J. Appl. Phys. **63**, 315 (1987).
[22]X. L. Wu and C. M. Lieber, Phys. Rev. Lett. **64**, 1150 (1990).
[23]C. G. Slough, W. W. McNairy, C. Wang, and R. V. Coleman, J. Vac. Sci. Technol. B **9**, 2 (1991); **9**, 1036 (1991).
[24]X. L. Wu and C. M. Lieber, J. Vac. Sci. Technol. B **9**, 1044 (1991).
[25]J. Tersoff, Phys. Rev. Lett. **57**, 440 (1986).

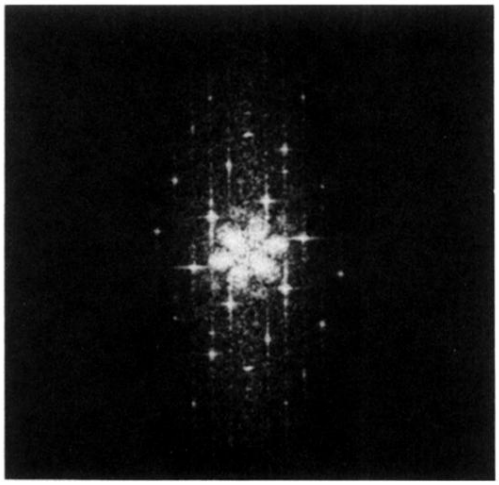

FIG. 10. Squared-amplitude two-dimensional Fourier transform corresponding to Fig. 8.

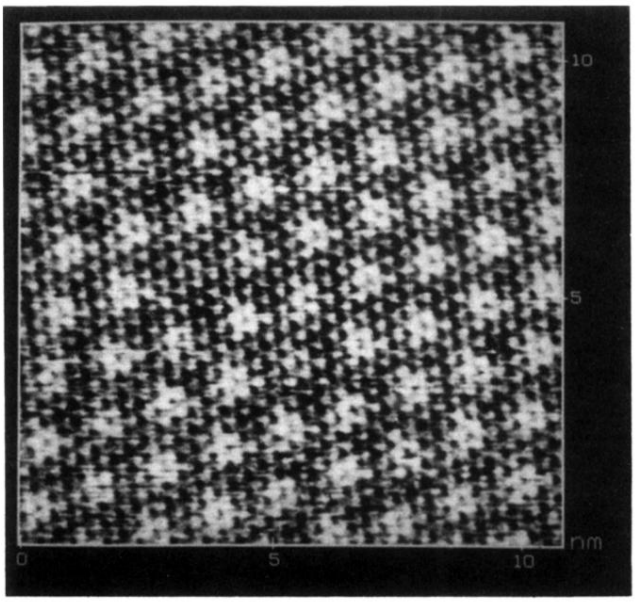

FIG. 3. STM constant-height image of $1T$-$TaSe_2$ at $V_{sample} - V_{tip} = 3.1$ mV and $I_{set\ point} = 2.4$ nA.

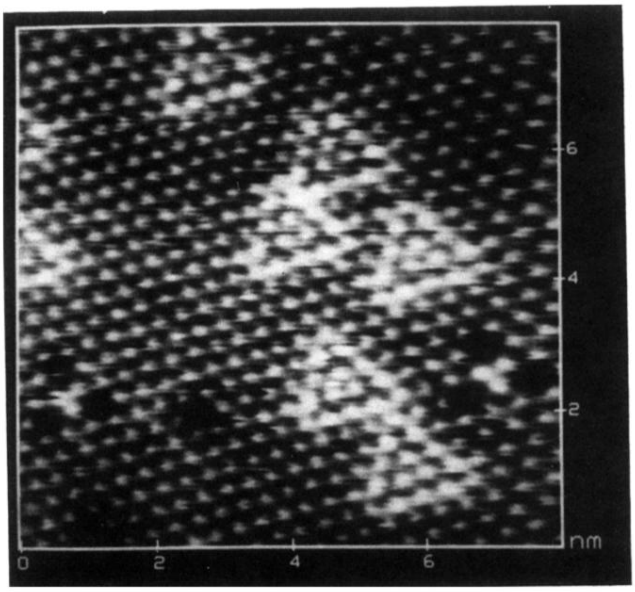

FIG. 4. STM constant-current image of $1T$-TiS_2 at $V_{\text{sample}} - V_{\text{tip}} = 25$ mV and $I_{\text{set point}} = 1.3$ nA.

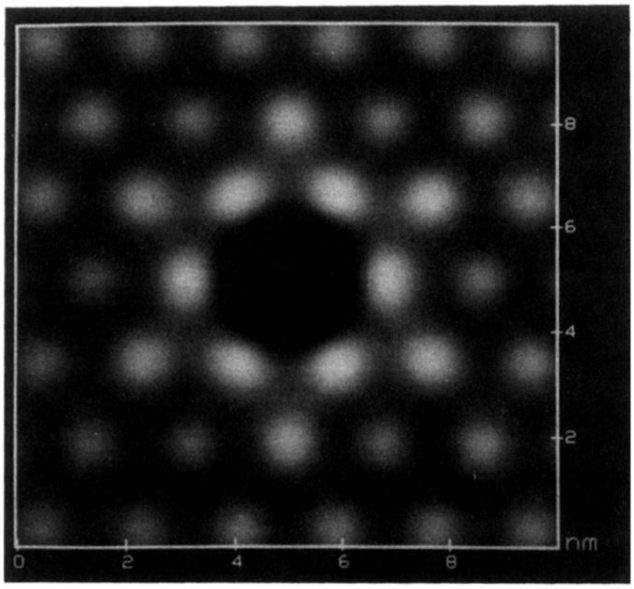

FIG. 5. Calculated STM image of a type-1 feature.

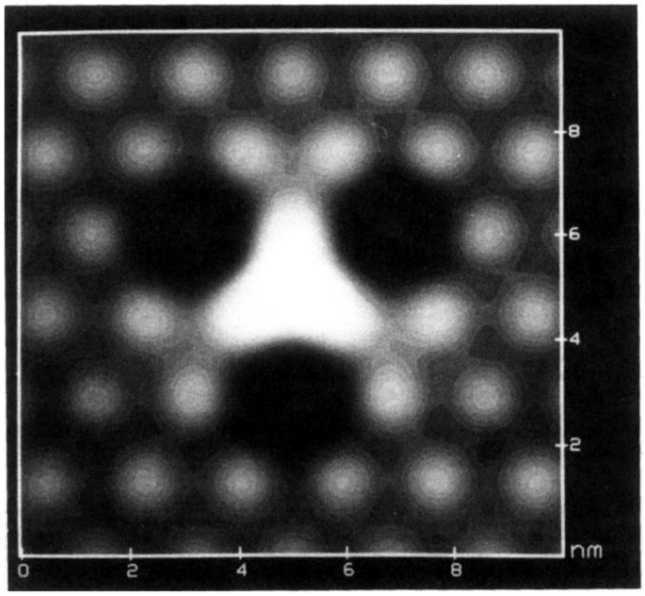

FIG. 6. Calculated STM image of a type-6 feature.

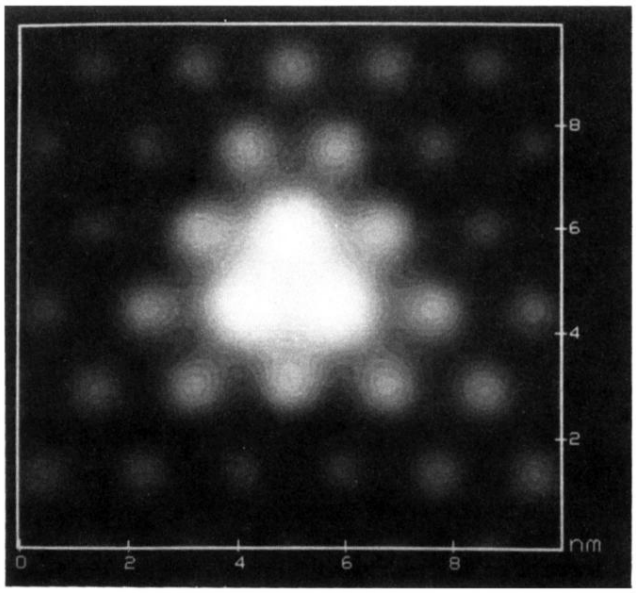

FIG. 7. Calculated STM image of a type-15 feature.

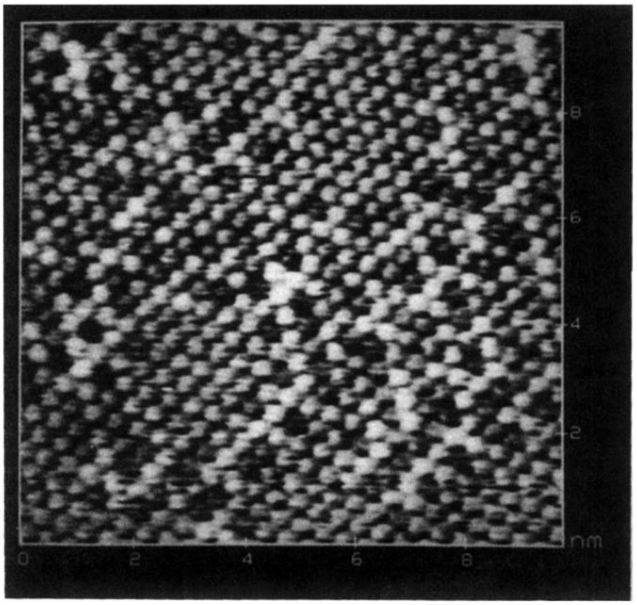

FIG. 8. STM constant-height image of $2H$-$NbSe_2$ at $V_{sample} - V_{tip} = 5.8$ mV and $I_{set\ point} = 1.0$ nA.

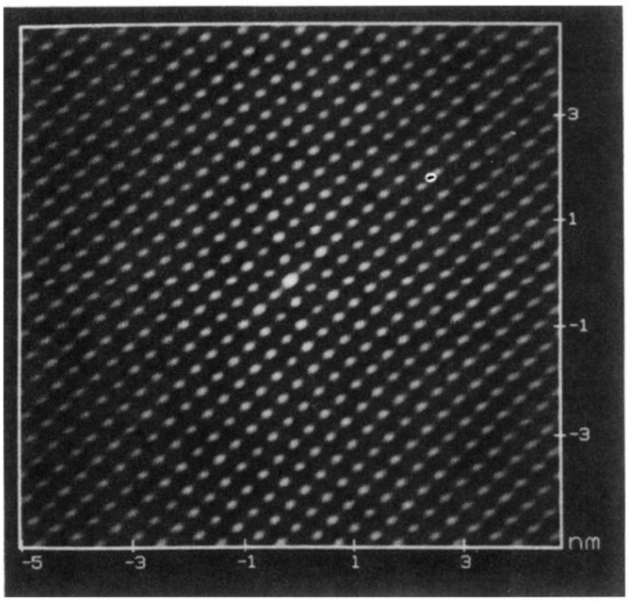

FIG. 9. Autocorrelation function corresponding to Fig. 8.